SIAM J. NUMER. ANAL.
Vol. 62, No. 3, pp. 1372–1393

© 2024 Society for Industrial and Applied Mathematics

Downloaded 06/21/24 to 60.29.153.12 . Redistribution subject to SIAM license or copyright; see https://epubs.siam.org/terms-privacy

INVERSE WAVE-NUMBER-DEPENDENT SOURCE PROBLEMS FOR THE HELMHOLTZ EQUATION[*]

HONGXIA GUO[†] AND GUANGHUI HU[‡]

Abstract. This paper is concerned with the multi-frequency factorization method for imaging the support of a wave-number-dependent source function. It is supposed that the source function is given by the inverse Fourier transform of some time-dependent source with a priori given radiating period. Using the multi-frequency far-field data at a fixed observation direction, we provide a computational criterion for characterizing the smallest strip containing the support and perpendicular to the observation direction. The far-field data from sparse observation directions can be used to recover a Θ-convex polygon of the support. The inversion algorithm is proven valid even with multi-frequency near-field data in three dimensions. The connections to time-dependent inverse source problems are discussed in the near-field case. Numerical tests in both two and three dimensions are implemented to show effectiveness and feasibility of the approach. This paper provides numerical analysis for a frequency-domain approach to recover the support of an admissible class of time-dependent sources.

Key words. inverse source problem, Helmholtz equation, multi-frequency data, wave-number-dependent sources, factorization method

MSC codes. 35R30, 65N21, 35P25

DOI. 10.1137/23M1572696

1. Introduction and problem formulation.

Consider the time-dependent acoustic wave radiating from a source term in an isotropic and homogeneous medium

$$\begin{aligned} \partial_t^2 U(x,t) &= \Delta U(x,t) + S(x,t), && (x,t)\in\mathbb{R}^3\times\mathbb{R}_+, \\ U(x,0) &= \partial_t U(x,0) = 0, && x\in\mathbb{R}^3, \end{aligned} \tag{1.1}$$

where $\operatorname{supp} S(x,t) = \overline{D}\times[t_{\min},t_{\max}]\subset\mathbb{R}^3\times\mathbb{R}_+$ with $t_{\max}>t_{\min}\geq 0$. The wave speed in the background medium has been normalized to be one. We suppose that $D\subset\mathbb{R}^3$ is a bounded Lipschitz domain such that $\mathbb{R}^3\backslash\overline{D}$ is connected and that $S(x,t)\in C([t_{\min},t_{\max}],L^\infty(D))$ is a real-valued function fulfilling the positivity constraint

$$S(x,t)\geq c_0>0 \qquad \text{a.e. } x\in\overline{D}, \quad t\in[t_{\min},t_{\max}]. \tag{1.2}$$

The above condition (1.2) implies that the location and shape of the time-dependent source support D does not vary along with the time variable. The time interval $[t_{\min},t_{\max}]\subset\mathbb{R}_+$ represents the duration period for source radiating. The solution U can be given explicitly as the convolution of the fundamental solution to the wave equation with the source term, that is,

$$U(x,t) = G(x,t)*S(x,t) := \int_{\mathbb{R}_+}\int_{\mathbb{R}^3} G(x-y;t-\tau)S(y,\tau)\,dy\,d\tau, \tag{1.3}$$

---

[*] Received by the editors May 22, 2023; accepted for publication (in revised form) March 7, 2024; published electronically June 6, 2024.
https://doi.org/10.1137/23M1572696

Funding: The work of the second author is partially supported by the National Natural Science Foundation of China (12071236) and the Fundamental Research Funds for Central Universities in China (63213025).

[†] School of Mathematical Sciences and LPMC, Nankai University, 300071 Tianjin, China (hxguo@nankai.edu.cn).

[‡] Corresponding author. School of Mathematical Sciences and LPMC, Nankai University, 300071 Tianjin, China (ghhu@nankai.edu.cn).

Copyright © by SIAM. Unauthorized reproduction of this article is prohibited.

Downloaded 06/21/24 to 60.29.153.12 . Redistribution subject to SIAM license or copyright; see https://epubs.siam.org/terms-privacy

where $G(x,t)=\frac{\delta(t-|x|)}{4\pi|x|}$ is the Green's function to the wave equation in 3D. Taking the inverse Fourier transform of $U(x,t)$ with respect to the time variable, one deduces from (1.3) that

$$w(x,k):=\frac{1}{\sqrt{2\pi}}\int_{\mathbb{R}}U(x,t)e^{\mathrm{i}kt}dt=\int_{\mathbb{R}^3}\Phi_k(x,y)f(y,k)\,dy, \tag{1.4}$$

where $\Phi_k(x,y)=\frac{e^{\mathrm{i}k|x-y|}}{4\pi|x-y|}$ and $f(y,k)$ denote respectively the inverse Fourier transforms of the fundamental solution $G(x-y;t)$ and $S(y,t)$. It is well known that $\Phi_k(x,y)$ satisfies the Sommerfeld radiation condition. By the assumption of S, we have

$$f(x,k)=\frac{1}{\sqrt{2\pi}}\int_{\mathbb{R}}S(x,t)e^{\mathrm{i}kt}dt=\frac{1}{\sqrt{2\pi}}\int_{t_{\min}}^{t_{\max}}S(x,t)e^{\mathrm{i}kt}dt, \tag{1.5}$$

which is compactly supported on $\overline{D}$ with respect to the space variables. Moreover, $f(\cdot,k)\in L^2(D)$ for any $k>0$. Therefore, it follows from (1.4) that $w(\cdot,k)\in H^2_{loc}(\mathbb{R}^3)$ satisfies

$$\Delta w(x,k)+k^2w(x,k)=-f(x,k),\quad x\in\mathbb{R}^3,\ k>0, \tag{1.6}$$

$$\lim_{r\to\infty}r(\partial_r w-\mathrm{i}kw)=0,\qquad r=|x|, \tag{1.7}$$

where the limit (1.7) holds uniformly in all directions $\hat{x}=x/|x|\in\mathbb{S}^2:=\{x\in\mathbb{R}^3: |x|=1\}$. The Sommerfeld radiation condition (1.7) gives rise to the following asymptotic behavior at infinity:

$$w(x)=\frac{e^{\mathrm{i}k|x|}}{4\pi|x|}\left\{w^\infty(\hat{x},k)+O\left(\frac{1}{|x|}\right)\right\}\quad\text{as}\quad |x|\to\infty, \tag{1.8}$$

where $w^\infty(\cdot,k)\in C^\infty(\mathbb{S}^2)$ is referred to as the far-field pattern (or scattering amplitude) of w. It is well known that the function $\hat{x}\mapsto w^\infty(\hat{x},k)$ is real analytic on $\mathbb{S}^2$, where $\hat{x}\in\mathbb{S}^2$ is usually called the observation direction.

By (1.4), the far-field pattern w^∞ of w can be expressed as

$$w^\infty(\hat{x},k)=\int_D e^{-\mathrm{i}k\hat{x}\cdot y}f(y,k)\,dy,\quad \hat{x}\in\mathbb{S}^2,\quad k>0. \tag{1.9}$$

Furthermore, substituting (1.5) into (1.9), we obtain the expression of the far-field pattern w^∞ in the frequency domain as follows:

$$w^\infty(\hat{x},k)=\frac{1}{\sqrt{2\pi}}\int_{t_{\min}}^{t_{\max}}\int_D e^{-\mathrm{i}k(\hat{x}\cdot y-t)}S(x,t)\,dy\,dt,\quad \hat{x}\in\mathbb{S}^2,\quad k>0. \tag{1.10}$$

Noting that the time-dependent source S is real valued, we have $f(x,-k)=\overline{f(x,k)}$ and thus $w^\infty(\hat{x},-k)=\overline{w^\infty(\hat{x},k)}$ for all $k>0$. Let $0\le k_{\min}<k_{\max}$ and denote by $(k_{\min},k_{\max})$ the bandwidth of wave-numbers of the Helmholtz equation. In this paper we are interested in the following inverse problem: determine the position and shape of the support D from knowledge of the multi-frequency far/near-field patterns $\{w^\infty(\hat{x}_j,k): k\in(k_{\min},k_{\max}),\, j=1,2,\ldots,J\}$.

If the source term is independent of frequencies (which corresponds to the critical case that $S(x,t)=s(x)\delta(t)$ and $f(x,k)=s(x)$), the far-field pattern given by

Copyright © by SIAM. Unauthorized reproduction of this article is prohibited.

Downloaded 06/21/24 to 60.29.153.12 . Redistribution subject to SIAM license or copyright; see https://epubs.siam.org/terms-privacy

(1.9) is nothing else but the Fourier transform of the space-dependent source term f at the Fourier variable $\xi = k\hat{x} \in \mathbb{R}^3$ multiplied by some constant. Since f is compactly supported in D, its Fourier transform is analytic in $\xi \in \mathbb{R}^3$. Hence, the far-field measurements over an interval of frequencies and observation directions uniquely determine the source function and also its support. A wide range of literature is devoted to inverse wavenumber-independent source problems with multi-frequency data, for example, uniqueness proofs and increasing stability analysis with near-field measurements [6, 7, 12, 15, 39] and a couple of numerical schemes such as the iterative method, Fourier method, and test-function method for recovering the source function [6, 8, 15, 45] and sampling-type methods for imaging the support [3, 17, 34]. On the other hand, the inverse source problem with the measurement data at a single frequency becomes severely ill-posed. It is impossible in general to determine a source function (even its support) from a single far-field pattern due to the existence of nonradiating sources; see, e.g., [11, 13, 14] for nonuniqueness examples. In a series papers by Kusiak and Sylvester [38, 43, 44], the concept of convex scattering support has been introduced to define the smallest convex set that carries a single far-field pattern. It was shown in [10, 25] that a convex-polygonal source support and an admissible class of analytic source functions can be uniquely determined by a single far-field pattern. Numerical schemes such as the enclosure method [29] and one-wave factorization method [40] were proposed for imaging the support of such convex-polygonal sources. The filtered backprojection method [20, 21] and a hybrid method involving iterative and range tests [2] were also investigated with a single far-field measurement.

In contrast to the vast literature for space-dependent source terms, little is known if the source function depends on both frequency/wave-number and spatial variables. Here we assume that the dependence on the frequency is unknown. One can see the essential difficulties from the expression (1.9), where the far-field pattern is no longer the Fourier transform of the source function. Hence, most existing methods cannot be straightforwardly carried over to frequency-number-dependent source terms. In this paper, we consider an inverse frequency-dependent source problem originating from inverse time-dependent source problems. The temporal function is supposed to be unknown, but the starting and terminal time points for radiating are given. Consequently, the source term takes a special integral form of the time-dependent source function (see (1.5)) with a priori given source radiating period $[t_{\min}, t_{\max}]$. This is motivated by the Fourier method of [26, 27, 28] for proving uniqueness in determining the source function of inhomogeneous hyperbolic equations with vanishing initial data. In these works the inverse time-dependent problems were reduced to equivalent problems in the time-harmonic regime with multi-frequency data. The proposed factorization scheme seems not applicable to general wave-number-dependent sources, because we do not know how to get a desirable factorization form of the far-field operator. Confined by such source functions, we think it is nontrivial to extend our method to inverse medium scattering problems with multi-frequency data. We refer the reader to [16, 18, 19, 23, 32, 33, 41] for the application of the sampling-type methods to nonlinear inverse problems modeled by the Helmholtz equation.

The multi-static factorization method [35, 37], which was proposed by Kirsch in 1998, provides a necessary and sufficient criterion for precisely characterizing the shape and location of a scattering obstacle, utilizing the multi-static spectral system of the far-field operator. The multi-frequency factorization method was rigorously justified in [17] for recovering the smallest strip $K_D^{(\hat{x})}$ that contains the support D

Copyright © by SIAM. Unauthorized reproduction of this article is prohibited.

Downloaded 06/21/24 to 60.29.153.12 . Redistribution subject to SIAM license or copyright; see https://epubs.siam.org/terms-privacy

of a wave-number-independent source and is orthogonal to the observation direction $\hat{x}$. Moreover, the Θ-convex polygon of the support can be recovered from the multi-frequency far-field data over sparse observation directions. The aim of this paper is to establish the analogue of the multi-frequency factorization method [17] for imaging the support of a wave-number-dependent source function of the form (1.5). We prove a new range identity for connecting ranges of the far-field operator F and the "data-to-pattern" operator L. This yields a computational criterion for characterizing the Θ-convex hull of D using the multi-frequency far-field data over sparse observation directions; see Theorem 4.2.

If the near-field measurement data are available in three dimensions, the reconstruction scheme can be used for recovering the minimum and maximum distance between the support and a measurement position. The connection between the near-field factorization method and the time-dependent wave radiating problems will be discussed in section 4. In two dimensions, the factorization method with far-field data still remains valid, but the near-field version no longer holds true, perhaps due to the lack of Huygens's principle. It is worth noting that the wave-number-dependence of sources makes this paper quite different from [17]. It is necessary to know the radiating period $[t_{\min}, t_{\max}]$ of the time-dependent source in advance. Physically, this can be explained by the fact that arrival and terminal time points of wave signals at an observation point are available; we refer the reader to section 4 for the physical interpretation. However, the a priori information on the radiating period $[t_{\min}, t_{\max}]$ can be relaxed to the condition that either $t_{\min}$ or $t_{\max}$ is known, and this will be studied in our future works. The reconstruction method considered here can be regarded as a frequency-domain method for recovering the support of a time-dependent source fulfilling the positivity condition (1.2). The novelty of this paper lies in the establishment of the multi-frequency factorization method for an inverse wave-number-dependent source problem. This has been achieved by considering a special kind of source term. The factorization scheme for general source terms, including inverse medium scattering problems, still remains open.

The remainder of the paper is organized as follows. In section 2, the concept of the multi-frequency far-field operator is introduced, and a new range identity is verified. Section 3 is devoted to the choice of test functions for characterizing the strip $K_D^{(\hat{x})}$ through the "data-to-pattern" operator L. In section 4 we define indicator functions using the far-field and near-field data measured at one or several observation directions/points. Numerical examples are reported in section 5. In [25] we also present analysis and numerics for imaging two disconnected supports.

Below we introduce some notation to be used throughout this paper. Unless otherwise stated, we always suppose that D is connected and bounded. Given $\hat{x} \in \mathbb{S}^2$, we define $\hat{x} \cdot D := \{t \in \mathbb{R} : t = \hat{x} \cdot y \text{ for some } y \in D\} \subset \mathbb{R}$. Hence, $(\inf(\hat{x} \cdot D), \sup(\hat{x} \cdot D))$ must be a finite and connected interval on the real axis. A ball centered at $y \in \mathbb{R}^3$ with the radius $\epsilon > 0$ will be denoted as $B_\epsilon(y)$. For brevity we write $B_\epsilon = B_\epsilon(0)$ when the ball is centered at the origin. Obviously, $\hat{x} \cdot B_\epsilon(y) = (\hat{x} \cdot y - \epsilon, \hat{x} \cdot y + \epsilon)$. In this paper the one-dimensional Fourier and inverse Fourier transforms are defined respectively by

$$(\mathcal{F}f)(k) = \frac{1}{\sqrt{2\pi}} \int_{\mathbb{R}} f(t) e^{-\mathrm{i}kt}\, dt, \quad (\mathcal{F}^{-1}v)(t) = \frac{1}{\sqrt{2\pi}} \int_{\mathbb{R}} v(k) e^{\mathrm{i}kt}\, dk.$$

Copyright © by SIAM. Unauthorized reproduction of this article is prohibited.

Downloaded 06/21/24 to 60.29.153.12 . Redistribution subject to SIAM license or copyright; see https://epubs.siam.org/terms-privacy

2. Factorization of far-field operator and a new range identity.

Following the ideas of [17], we introduce the central frequency k_c and half of the bandwidth of the given data as $k_c := (k_{\min} + k_{\max})/2$, $K := (k_{\max} - k_{\min})/2$. For every fixed $\hat{x} \in \mathbb{S}^2$, we define the far-field operator by

$$(F\phi)(\tau) = (F^{(\hat{x})}\phi)(\tau) := \int_0^K w^\infty(\hat{x}, k_c + \tau - s)\,\phi(s)\,ds, \quad \tau \in (0, K). \tag{2.1}$$

Since $w^\infty(\hat{x}, k)$ is analytic with respect to the wave number $k \in \mathbb{R}$, the operator $F^{(\hat{x})} : L^2(0, K) \to L^2(0, K)$ is bounded. For notational convenience we introduce the space $X_D := L^2(D \times (t_{\min}, t_{\max}))$. Denote by $\langle \cdot, \cdot \rangle_{X_D}$ the inner product over X_D. Below we shall prove a factorization of the far-field operator.

THEOREM 2.1. *We have $F = L\mathcal{T}L^*$, where $L = L_D^{(\hat{x})}$ is defined by*

$$(Lu)(\tau) = \int_{t_{\min}}^{t_{\max}} \int_D e^{-i\tau(\hat{x}\cdot y - t)} u(y, t)\,dydt, \qquad \tau \in (0, K), \tag{2.2}$$

for all $u \in X_D$, and $\mathcal{T} : X_D \to X_D$ is a multiplication operator defined by

$$(\mathcal{T}u)(y, t) := \frac{1}{\sqrt{2\pi}} e^{-ik_c(\hat{x}\cdot y - t)}\, S(y, t)\, u(y, t). \tag{2.3}$$

Proof. We first claim that the adjoint operator $L^* : L^2(0, K) \to X_D$ of L can be expressed by

$$(L^*\phi)(y, t) := \int_0^K e^{\mathrm{i}\tau(\hat{x}\cdot y - t)} \phi(\tau)\,d\tau, \quad \phi \in L^2(0, K). \tag{2.4}$$

Indeed, for $u \in X_D$ and $\phi \in L^2(0, K)$, it holds that

$$\begin{aligned}\langle Lu, \phi \rangle_{L^2(0,K)} &= \int_0^K \left(\int_{t_{\min}}^{t_{\max}} \int_D e^{-\mathrm{i}\tau(\hat{x}\cdot y - t)} u(y, t)\,dy\,dt \right) \overline{\phi(\tau)} d\tau \\ &= \int_{t_{\min}}^{t_{\max}} \int_D u(y, t) \left(\int_0^K \overline{\phi(\tau)\, e^{i\tau(\hat{x}\cdot y - t)}} d\tau \right) dy\,dt = \langle u, L^*\phi \rangle_{X_D},\end{aligned}$$

which implies (2.4). By the definition of $\mathcal{T}$,

$$(\mathcal{T}L^*\phi)(y, t) = \frac{1}{\sqrt{2\pi}} e^{-\mathrm{i}k_c(\hat{x}\cdot y - t)}\, S(y, t) \int_0^K e^{is(\hat{x}\cdot y - t)} \phi(s)\,ds, \quad \phi \in L^2(0, K).$$

Hence, combining (1.5), (2.2), and (2.1) yields

$$\begin{aligned}(L\mathcal{T}L^*\phi)(\tau) &= \int_{t_{\min}}^{t_{\max}} \int_D e^{-\mathrm{i}\tau(\hat{x}\cdot y - t)} \left(\frac{1}{\sqrt{2\pi}} e^{-\mathrm{i}k_c(\hat{x}\cdot y - t)}\, S(y, t) \int_0^K e^{\mathrm{i}s(\hat{x}\cdot y - t)} \phi(s)\,ds \right) dy\,dt \\ &= \frac{1}{\sqrt{2\pi}} \int_0^K \int_D e^{-\mathrm{i}(k_c + \tau - s)\hat{x}\cdot y} \phi(s) \left(\int_{t_{\min}}^{t_{\max}} S(y, t) e^{\mathrm{i}(k_c + \tau - s)t}\,dt \right) dy\,ds \\ &= \frac{1}{\sqrt{2\pi}} \int_0^K \int_D e^{-\mathrm{i}(k_c + \tau - s)\hat{x}\cdot y} \phi(s)\, f(y, k_c + \tau - s)\,dy\,ds = (F\phi)(\tau).\end{aligned}$$

This proves the factorization $F = L\mathcal{T}L^*$. ∎

The operator $L_D^{(\hat{x})}$ maps a time-dependent source function $S(x, t)$ supported on $\overline{D} \times [t_{\min}, t_{\max}]$ to multi-frequency far-field patterns at the observation direction $\hat{x}$, that is, $w^\infty(\hat{x}, \cdot) = (L_D^{(\hat{x})} S)(\cdot)$. It will be referred to as the "data-to-pattern" operator within this paper. Denote by $\text{Range}(L_D^{(\hat{x})})$ the range of the operator $L_D^{(\hat{x})}$ (see (2.2)) acting on X_D.

Copyright © by SIAM. Unauthorized reproduction of this article is prohibited.

Downloaded 06/21/24 to 60.29.153.12 . Redistribution subject to SIAM license or copyright; see https://epubs.siam.org/terms-privacy

LEMMA 2.1. *The operator* $L_D^{(\hat{x})}: X_D \to L^2(0,K)$ *is compact with dense range.*

Proof. For any $u \in X_D$, it holds that $L_D^{(\hat{x})} u \in H^1(0,K)$ by definition (2.2). Since $H^1(0,K)$ is compactly embedded into $L^2(0,K)$, we get the compactness of $L_D^{(\hat{x})}$. To prove the denseness of $\mathrm{Range}(L_D^{(\hat{x})})$ in $L^2(0,K)$, we only need to prove the injectivity of $(L_D^{(\hat{x})})^*$. If $(L_D^{(\hat{x})})^* \phi = 0$ for some $\phi \in L^2(0,K)$, from (2.4) it follows that

$$\int_0^K e^{\mathrm{i}\tau(\hat{x}\cdot y - t)} \phi(\tau)\, d\tau = 0 \quad \text{in} \quad X_D.$$

Denote by $\tilde{\phi}$ the extension of ϕ by zero from $(0,K)$ to $\mathbb{R}$. The previous relation implies

$$0 = \frac{1}{\sqrt{2\pi}} \int_{\mathbb{R}} e^{\mathrm{i}\tau(\hat{x}\cdot y - t)} \tilde{\phi}(\tau)\, d\tau = (\mathcal{F}^{-1}\tilde{\phi})(\xi),$$

where $\xi = \hat{x}\cdot y - t \in (\inf(\hat{x}\cdot D) - t_{\max}, \sup(\hat{x}\cdot D) - t_{\min})$. The analyticity of $(\mathcal{F}^{-1}\tilde{\phi})(\xi)$ in $\xi \in \mathbb{R}$ yields the identical vanishing of the inverse Fourier transform of $\tilde{\phi}$. This proves $\phi = 0$ and thus the injectivity of $(L_D^{(\hat{x})})^*$. ☐

Now we want to connect the ranges of F and L. The existing range identities (see, e.g., [37, Theorem 2.15] and [36, Theorems 4.1 and 4.4]) are not applicable to our case, because the real part of the middle operator $\mathcal{T}$ (see (2.3)) cannot be decomposed into the sum of a positive and a compact operator. Nevertheless, the multiplication form of the middle operator motivates us to establish a new range identity. We first recall that, for a bounded operator $F: Y \to Y$ in a Hilbert space Y, its real and imaginary parts are defined respectively by $\mathrm{Re}\, F = (F + F^*)/2$, $\mathrm{Im}\, F = (F - F^*)/(2i)$, which are both self-adjoint operators. Furthermore, by spectral representation we define the self-adjoint and positive operator $|\mathrm{Re}\, F|$ as

$$|\mathrm{Re}\, F| = \int_{\mathbb{R}} |\lambda|\, dE_\lambda \qquad \text{if} \quad \mathrm{Re}\, F = \int_{\mathbb{R}} \lambda\, dE_\lambda.$$

The self-adjoint and positive operator $|\mathrm{Im}\, F|$ can be defined analogously. In this paper the operator $F_\#$ is defined as $F_\# := |\mathrm{Re}\, F| + |\mathrm{Im}\, F|$. If $F_\#$ is self-adjoint and positive, its square root $F_\#^{1/2}$ is well defined. We need the following auxiliary result from functional analysis.

THEOREM 2.2. *Let* X *and* Y *be Hilbert spaces and let* $F: Y \to Y$, $L: X \to Y$, *and* $\mathcal{T}: X \to X$ *be bounded linear operators such that* $F = L\mathcal{T}L^*$. *We make the following assumptions:*

(i) L *is compact with dense range and thus* L^* *is compact and one-to-one.*

(ii) $\mathrm{Re}\,\mathcal{T}$ *and* $\mathrm{Im}\,\mathcal{T}$ *are both one-to-one and the operator* $\mathcal{T}_\# = |\mathrm{Re}\,\mathcal{T}| + |\mathrm{Im}\,\mathcal{T}|:$ $X \to X$ *is coercive, i.e., there exists* $c > 0$ *with*

$$\langle \mathcal{T}_\# \varphi, \varphi \rangle_X \geq c\, ||\varphi||_X^2 \quad \textit{for all} \quad \varphi \in X.$$

Then the operator $F_\#$ *is positive and the ranges of* $F_\#^{1/2}: Y \to Y$ *and* $L: X \to Y$ *coincide.*

Proof. We first recall from Part A in the proof of [37, Theorem 2.15] that it is sufficient to assume that $L^*: Y \to X$ has dense range in X. If otherwise, we may replace X by the closed subspace $\overline{\mathrm{Range}(L^*)}$ by using the orthogonal projection from X onto $\overline{\mathrm{Range}(L^*)}$. Below we shall prove the decomposition $F_\# = L\mathcal{T}_\# L^*$. For this purpose we only need to show

Copyright © by SIAM. Unauthorized reproduction of this article is prohibited.

Downloaded 06/21/24 to 60.29.153.12 . Redistribution subject to SIAM license or copyright; see https://epubs.siam.org/terms-privacy

$$|\mathrm{Re}\, F| = L\, |\mathrm{Re}\, \mathcal{T}|\, L^*, \qquad |\mathrm{Im}\, F| = L\, |\mathrm{Im}\, \mathcal{T}|\, L^*. \tag{2.5}$$

It suffices to consider the real part of F, because the imaginary part can be treated similarly. Since $\mathrm{Re}\, F = L\, (\mathrm{Re}\, \mathcal{T})\, L^*$ is self-adjoint, it has a complete orthonormal eigensystem $\{(\lambda_j, \psi_j) : j \in \mathbb{N}\}$. Hence, the space Y can be split into two closed orthogonal subspaces $Y = Y^- \oplus Y^+$ with

$$Y^- = \mathrm{span}\{\psi_j : \lambda_j \leq 0\}, \quad Y^+ = \mathrm{span}\{\psi_j : \lambda_j \geq 0\}.$$

We note that $Y^- \cap Y^+ = \{0\}$, since $\lambda_j = 0$ yields $\psi_j = 0$. It is obvious that $\langle (\mathrm{Re}\, F)\psi, \psi\rangle_Y$ is nonnegative on Y^+ and nonpositive on Y^-.

Consequently, $\langle (\mathrm{Re}\, \mathcal{T})\phi, \phi\rangle_X$ is nonnegative on $U^+ := \overline{L^*(Y^+)}$ and is nonpositive on $U^- := \overline{L^*(Y^-)}$, because

$$\langle (\mathrm{Re}\, \mathcal{T})\phi, \phi\rangle_X = \langle (\mathrm{Re}\, \mathcal{T})L^*(\psi^\pm), L^*(\psi^\pm)\rangle_X = \langle (\mathrm{Re}\, F)(\psi^\pm), \psi^\pm\rangle_Y \lesseqgtr 0, \tag{2.6}$$

where $\phi = L^*(\psi^\pm)$ with $\psi^\pm \in Y^\pm$. This implies that

$$\langle (\mathrm{Re}\, \mathcal{T})\phi, \phi\rangle_X = 0 \qquad \text{if} \quad \phi \in U^+ \cap U^-. \tag{2.7}$$

For $\phi \in U^+ \cap U^-$, we have $\phi^\pm + t\phi \in U^\pm$ for all $\phi^\pm \in U^\pm$ and for all $t \in \mathbb{C}$. This together with the relation (2.7) leads to $\langle (\mathrm{Re}\, \mathcal{T})\phi, \phi^\pm\rangle_X = 0$; see Part C in the proof of [37, Theorem 2.15]. From this we deduce that $(\mathrm{Re}\, \mathcal{T})\phi = 0$. Since $\mathrm{Re}\, \mathcal{T}$ is one-to-one, we thus obtain $\phi = 0$. In view of the denseness of the range of L^*, this proves the orthogonal decomposition $X = U^+ \oplus U^-$.

To proceed with the proof, we denote by $P_Y^\pm$ the orthogonal projectors from Y onto $Y^\pm$. Since $\mathrm{Re}\, F$ is invariant on both Y^+ and Y^-, there holds

$$|\mathrm{Re}\, F| = (P^+ - P^-)(\mathrm{Re}\, F) = (\mathrm{Re}\, F)(P^+ - P^-) = L\, (\mathrm{Re}\, \mathcal{T})\, L^*\, (P^+ - P^-). \tag{2.8}$$

Introduce the orthogonal projections $Q_U^\pm : X \to U^\pm$. It is then easy to conclude the relations $(\mathrm{Re}\, \mathcal{T})\, L^*\, P_Y^\pm = (\mathrm{Re}\, \mathcal{T})\, Q_U^\pm L^*$. Therefore, using (2.8) and (2.6), we get

$$|\mathrm{Re}\, F| = L\, (\mathrm{Re}\, \mathcal{T})\, L^*\, (P_Y^+ - P_Y^-) = L\, [(\mathrm{Re}\, \mathcal{T})(Q_U^+ - Q_U^-)]\, L^* = L\, |\mathrm{Re}\, \mathcal{T}|\, L^*,$$

which proves the first relation in (2.5) and thus also the decomposition $F_\# = L\mathcal{T}_\# L^*$. By the second assumption (ii), we obtain the positivity of $F_\#$. By the coercivity of $\mathcal{T}_\#$, we can define the square root operator $\mathcal{T}_\#^{1/2}$, which is also coercive and self-adjoint. Thus, we have a decomposition of $F_\#$ in the form

$$F_\# = (L\mathcal{T}_\#^{1/2})\, (L\mathcal{T}_\#^{1/2})^* = F_\#^{1/2}\, (F_\#^{1/2})^*.$$

Application of [37, Theorem 1.21] gives $(F_\#^{1/2}) = \mathrm{Range}\, (L)$. ∎

To apply Theorem 2.2 to our inverse problem, we set $F = F_D^{(\hat{x})}$, $X = X_D$, $Y = L^2(0, K)$ and let $\mathcal{T}$ be the multiplication operator of (2.3). Since the source function $S(x,t)$ is real valued, it follows from (2.3) that

$$\begin{aligned}
(\mathrm{Re}\, \mathcal{T})\, u &= \frac{1}{\sqrt{2\pi}} \cos\big(k_c(\hat{x}\cdot y - t)\big)\, S(y,t)\, u(y,t),\\
(\mathrm{Im}\, \mathcal{T})\, u &= \frac{1}{\sqrt{2\pi}} \sin\big(k_c(\hat{x}\cdot y - t)\big)\, S(y,t)\, u(y,t),
\end{aligned}$$

Copyright © by SIAM. Unauthorized reproduction of this article is prohibited.

Downloaded 06/21/24 to 60.29.153.12 . Redistribution subject to SIAM license or copyright; see https://epubs.siam.org/terms-privacy

both of which are one-to-one operators from X_D onto X_D. The coercivity assumption on S yields the coercivity of $\mathcal{T}_\#$, that is,

$$\begin{aligned}\langle \mathcal{T}_\# u, u\rangle &= \int_{t_{\min}}^{t_{\max}} \int_D \frac{1}{\sqrt{2\pi}} \Big(|\cos\big(k_c(\hat{x}\cdot y - t)\big)| + |\sin\big(k_c(\hat{x}\cdot y - t)\big)| \Big) S(y,t)\, |u(y,t)|^2\, dy dt \\ &\geq \frac{1}{\sqrt{2\pi}} \int_{t_{\min}}^{t_{\max}} \int_D S(y,t)\, |u(y,t)|^2\, dydt \geq \frac{1}{\sqrt{2\pi}} c_0\, ||u||^2_{X_D}.\end{aligned}$$

As a consequence of Theorem 2.2, we obtain

$$\text{Range}\,[(F_D^{(\hat{x})})_\#^{1/2}] = \text{Range}\,(L_D^{(\hat{x})}) \quad \text{for all} \quad \hat{x} \in \mathbb{S}^2. \tag{2.9}$$

Let $\chi(k) \in L^2(0,K)$ be some test function. Denote by $(\lambda_n^{(\hat{x})}, \psi_n^{(\hat{x})})$ an eigensystem of the positive and self-adjoint operator $(F_D^{(\hat{x})})_\#$, which is uniquely determined by the multi-frequency far-field patterns $\{w^\infty(\hat{x},k) : k \in (k_{\min}, k_{\max})\}$. Applying Picard's theorem and Theorem 2.2, we obtain

$$\chi \in \text{Range}(L_D^{(\hat{x})}) \quad \text{if and only if} \quad \sum_{n=1}^{\infty} \frac{|\langle \chi, \psi_n^{(\hat{x})}\rangle|^2}{|\lambda_n^{(\hat{x})}|} < \infty. \tag{2.10}$$

To establish the factorization method, we now need to choose a suitable class of test functions, which usually rely on a sample variable in $\mathbb{R}^3$. The inclusion relationship between the test function and Range$(L_D^{(\hat{x})})$ should be associated with the inclusion relationship between the corresponding sample variable and the region D.

Remark 2.1. In the special case that $k_{\min} = 0$, we can also apply the range identity of [36, Theorem 4.1] to get (2.9). In fact, since $w^\infty(\hat{x}, -k) = \overline{w^\infty(\hat{x},k)}$, we may extend the bandwidth from $(0, k_{\max})$ to $(-k_{\max}, k_{\max})$. Hence, one deduces from these new measurement data with $k_{\min} = -k_{\max}$ that $k_c = 0$ and $K = k_{\max}$. Consequently, the middle operator $\mathcal{T}$ is self-adjoint, due to the multiplication form $\mathcal{T}u = S\,u$ for $u \in X_D$. This implies that $F_D^{(\hat{x})}$ is also self-adjoint. Moreover, $F_D^{(\hat{x})}$ and $\mathcal{T}$ are both positive definite under the assumption (1.2) and thus $(F_D^{(\hat{x})})_\# = F_D^{(\hat{x})}$, $\mathcal{T}_\# = \mathcal{T}$. The range identity stated in Theorem 2.2 allows us to handle a more general class of wave-number bands, in particular an interval of wave-numbers bounded away from zero.

3. Range of $L_D^{(\hat{x})}$ and test functions.

In this section we choose a proper class of test functions to characterize the range of $L_D^{(\hat{x})}$. Throughout the paper we set $T := t_{\max} - t_{min} > 0$.

LEMMA 3.1. *Let $D_1, D_2 \subset \mathbb{R}^3$ be bounded domains such that $\hat{x}\cdot D_1 \cap \hat{x}\cdot D_2 = \emptyset$. Suppose one of the following relations holds:*

$$\inf(\hat{x}\cdot D_1) - \sup(\hat{x}\cdot D_2) > T, \quad \inf(\hat{x}\cdot D_2) - \sup(\hat{x}\cdot D_1) > T. \tag{3.1}$$

Then Range$(L_{D_1}^{(\hat{x})}) \cap$ Range$(L_{D_2}^{(\hat{x})}) = \{0\}$*, that is, the ranges of $L_{D_j}^{(\hat{x})}$ over X_{D_1} and X_{D_2} have trivial intersections.*

Proof. Let $f_j \in X_{D_j}$ be such that $L_{D_1}^{(\hat{x})} f_1 = L_{D_2}^{(\hat{x})} f_2 := \mathcal{G}(\cdot, \hat{x})$. By the definition of $L_D^{(\hat{x})}$ (see (2.2)), the function

$$\tau \mapsto \mathcal{G}(\tau, \hat{x}) = \int_{t_{\min}}^{t_{\max}} \int_{D_1} e^{-i\tau(\hat{x}\cdot y - t)} f_1(y,t)\, dydt = \int_{t_{\min}}^{t_{\max}} \int_{D_2} e^{-i\tau(\hat{x}\cdot y - t)} f_2(y,t)\, dydt$$

Copyright © by SIAM. Unauthorized reproduction of this article is prohibited.

Downloaded 06/21/24 to 60.29.153.12 . Redistribution subject to SIAM license or copyright; see https://epubs.siam.org/terms-privacy

belongs to $L^2(0,K)$. Since $\mathcal{G}(\cdot,\hat{x})$ is analytic, the previous relation is valid for all $\tau\in\mathbb{R}$. Extending f_j by zero from $(t_{\min},t_{\max})$ to $\mathbb{R}$ and letting $\xi=\hat{x}\cdot y-t$, we can rewrite the integrals over D_j as

$$\int_{D_j} e^{-\mathrm{i}\tau(\hat{x}\cdot y-t)}f_j(y,t)\,dy=\int_{\mathbb{R}} e^{-\mathrm{i}\tau\xi}\int_{\Gamma_j(\xi+t,\hat{x})} f_j(y,t)ds(y)\,d\xi,$$

where $\Gamma_j(t,\hat{x})\subset D_j$ is defined as

$$\Gamma_j(t,\hat{x}):=\{y\in D_j:\hat{x}\cdot y=t\}\subset\mathbb{R}^3,\quad t\in\mathbb{R},\quad j=1,2.$$

This implies that the function $\mathcal{G}(\cdot,\hat{x})$ is the Fourier transform of g_j:

$$\mathcal{G}(\tau,\hat{x})=\int_{\mathbb{R}} e^{-\mathrm{i}\tau\xi}g_j(\xi,\hat{x})\,d\xi,\qquad \tau\in\mathbb{R},\tag{3.2}$$

with

$$g_j(\xi,\hat{x}):=\int_{t_{\min}}^{t_{\max}}\int_{\Gamma_j(\xi+t,\hat{x})} f_j(y,t)ds(y)dt=\int_{\xi+t_{\min}}^{\xi+t_{\max}}\int_{\Gamma_j(t,\hat{x})} f_j(y,t-\xi)ds(y)dt$$

for $j=1,2$. By the arbitrariness of $\tau\in\mathbb{R}$, we get from (3.2) that $g_1(\xi,\hat{x})=g_2(\xi,\hat{x})$ for all $\xi\in\mathbb{R}$. On the other hand, observing that

$$\Gamma_j(t,\hat{x})=\emptyset\qquad\text{if}\quad t>\sup(\hat{x}\cdot D_j)\quad\text{or}\quad t<\inf(\hat{x}\cdot D_j),$$

we have

$$g_j(\xi,\hat{x})=0\qquad\text{if}\quad \xi+t_{\min}>\sup(\hat{x}\cdot D_j)\quad\text{or}\quad \xi+t_{\max}<\inf(\hat{x}\cdot D_j).$$

This implies

$$\operatorname{supp} g_j(\cdot,\hat{x})\subset\Big(\inf(\hat{x}\cdot D_j)-t_{\max},\,\sup(\hat{x}\cdot D_j)-t_{\min}\Big),\quad j=1,2,$$

By the conditions in (3.1), it is clear that one of the following relations holds:

$$\begin{aligned}\inf(\hat{x}\cdot D_1)-t_{\max}&>\sup(\hat{x}\cdot D_2)-t_{\min},\\ \inf(\hat{x}\cdot D_2)-t_{\max}&>\sup(\hat{x}\cdot D_1)-t_{\min},\end{aligned}$$

leading to $g_1(\xi,\hat{x})=g_2(\xi,\hat{x})\equiv 0$ for all $\xi\in\mathbb{R}$ in any case. Recalling (3.2), we obtain $L_{D_1}^{(\hat{x})}f_1=L_{D_2}^{(\hat{x})}f_2\equiv 0$. ☐

As a consequence of the proof of Lemma 3.1, we can get information on the supporting interval of the inverse Fourier transform of $L_D^{(\hat{x})}f$ for $f\in X_D$ as follows.

Corollary 3.1. *Let $D\subset\mathbb{R}^3$ be a bounded domain and $t_{\max}>t_{\min}$. Define*

$$\mathcal{G}(\tau,\hat{x}):=\int_{t_{\min}}^{t_{\max}}\int_D e^{-i\tau(\hat{x}\cdot y-t)}f(y,t)\,dydt,\qquad f\in X_D.$$

Then the support of the inverse Fourier transform of $\mathcal{G}(\cdot,\hat{x})$ is contained in the interval $\big(\inf(\hat{x}\cdot D)-t_{\max},\,\sup(\hat{x}\cdot D)-t_{\min}\big)$.

For any $y\in\mathbb{R}^3$ and $\epsilon>0$, define the test function $\phi_{y,\epsilon}^{(\hat{x})}\in L^2(0,K)$ by

$$\phi_{y,\epsilon}^{(\hat{x})}(k)=\frac{1}{T\,|B_\epsilon(y)|}\int_{t_{\min}}^{t_{\max}}\int_{B_\epsilon(y)} e^{-\mathrm{i}k(\hat{x}\cdot z-t)}dzdt,\qquad k\in(0,K),\tag{3.3}$$

Copyright © by SIAM. Unauthorized reproduction of this article is prohibited.

Downloaded 06/21/24 to 60.29.153.12 . Redistribution subject to SIAM license or copyright; see https://epubs.siam.org/terms-privacy

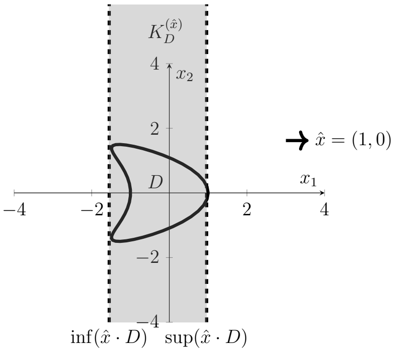

FIG. 1. *Illustration of the strip* $K_D^{(\hat x)}$ *with* $\hat x = (1,0)$.

where $|B_\epsilon(y)| = 4/3\pi\epsilon^3$ denotes the volume of the ball $B_\epsilon(y) \subset \mathbb{R}^3$. As $\epsilon \to 0$, there holds the convergence

$$\phi_{y,\epsilon}^{(\hat x)}(k) \to \phi_y^{(\hat x)}(k) := \frac{1}{T}\left(\int_{t_{\min}}^{t_{\max}} e^{\mathrm{i}kt}dt\right) e^{-\mathrm{i}k\hat x\cdot y}. \tag{3.4}$$

Below we describe the supporting interval of the inverse Fourier transform of the test functions defined by (3.3).

LEMMA 3.2. *For* $\epsilon > 0$, *we have*

$$[\mathcal{F}^{-1}\phi_{y,\epsilon}^{(\hat x)}](\xi) > 0 \quad \textit{if} \quad \xi \in (\hat x\cdot y - \epsilon - t_{\max},\, \hat x \cdot y + \epsilon - t_{\min}), \tag{3.5}$$

$$[\mathcal{F}^{-1}\phi_{y,\epsilon}^{(\hat x)}](\xi) = 0 \quad \textit{if} \quad \xi \notin (\hat x\cdot y - \epsilon - t_{\max},\, \hat x \cdot y + \epsilon - t_{\min}). \tag{3.6}$$

Proof. As done in (3.2), we can rewrite $\phi_{y,\epsilon}^{(\hat x)}$ as the Fourier transform of $g_\epsilon(\xi, \hat x)$:

$$\phi_{y,\epsilon}^{(\hat x)}(\tau) = \int_{\mathbb{R}} e^{-\mathrm{i}\tau\xi} g_\epsilon(\xi,\hat x)\,d\xi, \quad g_\epsilon(\xi,\hat x) = \frac{1}{T|B_\epsilon(y)|}\int_{\xi+t_{\min}}^{\xi+t_{\max}}\int_{\Gamma(t,\hat x)} ds(z)dt,$$

with $\Gamma(t,\hat x) = \{z \in B_\epsilon(y) : \hat x \cdot z = t\}$. Hence, $\mathcal{F}^{-1}\phi_{y,\epsilon}^{(\hat x)} = \sqrt{2\pi}\, g_\epsilon(\cdot,\hat x)$. Observing that

$$\sup\left(\hat x \cdot B_\epsilon(y)\right) = \hat x \cdot y + \epsilon, \quad \inf\left(\hat x \cdot B_\epsilon(y)\right) = \hat x\cdot y - \epsilon,$$

we obtain (3.5) and (3.6) from the expression of $g_\epsilon(\cdot,\hat x)$. ☐

Introduce the strip (see Figure 1)

$$K_D^{(\hat x)} := \{y \in \mathbb{R}^3 : \inf(\hat x \cdot D) < \hat x \cdot y < \sup(\hat x \cdot D)\} \subset \mathbb{R}^3. \tag{3.7}$$

The set $K_D^{(\hat x)} \subset \mathbb{R}^3$ represents the smallest strip containing D and perpendicular to the vector $\hat x \in \mathbb{S}^2$. We shall establish a computational criterion for imaging $K_D^{(\hat x)}$ from the multi-frequency far-field data $u^\infty(\hat x, k)$ with $k \in (k_{\min}, k_{\max})$.

LEMMA 3.3. (i) *For* $y \in K_D^{(\hat x)}$, *there exists* $\epsilon_0 > 0$ *such that* $\phi_{y,\epsilon}^{(\hat x)} \in \mathrm{Range}(L_D^{(\hat x)})$ *for all* $\epsilon \in (0, \epsilon_0)$.

(ii)*If* $y \notin K_D^{(\hat x)}$, *we have* $\phi_{y,\epsilon}^{(\hat x)} \notin \mathrm{Range}(L_D^{(\hat x)})$ *for all* $\epsilon > 0$.

Copyright © by SIAM. Unauthorized reproduction of this article is prohibited.

Proof. (i) If $\hat{x}\cdot y\in\hat{x}\cdot D$, there must exist some $z\in D$ and $\epsilon_0>0$ such that $\hat{x}\cdot y=\hat{x}\cdot z$ and $B_\epsilon(z)\subset D$ for all $\epsilon\in(0,\epsilon_0)$. Moreover, we have $\phi_{y,\epsilon}^{(\hat{x})}=\phi_{z,\epsilon}^{(\hat{x})}$. Set

$$u(x,t):=\begin{cases}\frac{1}{|B_\epsilon(z)|\,T} & \text{if}\, x\in B_\epsilon(z), t\in(t_{\min},t_{\max}),\\ 0 & \text{if otherwise.}\end{cases}$$

It is obvious that $u(x,t)\in L^2(D\times(t_{\min},t_{\max})$. By the definition of $L_D^{(\hat{x})}$ (see (2.2)), it is easy to see that $\phi_{z,\epsilon}^{(\hat{x})}=L_D^{(\hat{x})}u$.

(ii) Given $y\notin K_D^{(\hat{x})}$, we suppose on the contrary that $\phi_{y,\epsilon}^{(\hat{x})}=L_D^{(\hat{x})}f$ with some $f\in L^2(D\times(t_{\min},t_{\max}))$, i.e.,

$$\phi_{y,\epsilon}^{(\hat{x})}(\tau)=\int_{t_{\min}}^{t_{\max}}\int_D e^{-i\tau(\hat{x}\cdot z-t)}f(z,t)\,dzdt,\qquad \tau\in(0,K). \tag{3.8}$$

By the analyticity in τ, the above relation can be extended to $\tau\in\mathbb{R}$. Hence, the supporting intervals of the inverse Fourier transform of both sides of (3.8) must coincide. Using (3.5) and Corollary 3.1, we obtain

$$(\hat{x}\cdot y-\epsilon-t_{\max},\,\hat{x}\cdot y+\epsilon-t_{\min})\subset(\inf(\hat{x}\cdot D)-t_{\max},\,\sup(\hat{x}\cdot D)-t_{\min})\,,$$

leading to

$$\inf(\hat{x}\cdot D)+\epsilon\le\hat{x}\cdot y\le\sup(\hat{x}\cdot D)-\epsilon\quad\text{for all}\,\epsilon>0. \tag{3.9}$$

This implies that $y\in K_D^{(\hat{x})}$, a contradiction to the assumption $y\notin K_D^{(\hat{x})}$. This proves $\phi_{y,\epsilon}^{(\hat{x})}\notin\mathrm{Range}(L_D^{(\hat{x})})$ for all $\epsilon>0$. ∎

4. Indicator functions with multi-frequency far/near-field data.

By Lemma 3.3, the functions $\phi_{y,\epsilon}^{(\hat{x})}$ with a small $\epsilon>0$ can be taken as test functions to characterize D through (2.10). We first consider the indicator function involving $\phi_{y,\epsilon}^{(\hat{x})}$:

$$W_\epsilon^{(\hat{x})}(y):=\left[\sum_{n=1}^{\infty}\frac{|\langle\phi_{y,\epsilon}^{(\hat{x})},\psi_n^{(\hat{x})}\rangle|^2_{L^2(0,K)}}{|\lambda_n^{(\hat{x})}|}\right]^{-1},\ y\in\mathbb{R}^3. \tag{4.1}$$

The analogue of (4.1) was used in [17] for imaging the support of a wave-number-independent source function. Combining Theorem 2.2 and Lemma 3.3 yields the following theorem.

THEOREM 4.1. (i) *If $y\in K_D^{(\hat{x})}$, there exists $\epsilon_0>0$ such that $W_\epsilon^{(\hat{x})}(y)>0$ for all $\epsilon\in(0,\epsilon_0)$.*

(ii) *If $y\notin K_D^{(\hat{x})}$, there holds $W_\epsilon^{(\hat{x})}(y)=0$ for all $\epsilon>0$.*

Since $\phi_{y,\epsilon}^{(\hat{x})}$ convergences uniformly to $\phi_y^{(\hat{x})}$ over the finite wave-number interval $[k_{\min},k_{\max}]$, we shall use the limiting function $\phi_y^{(\hat{x})}$ in place of $\phi_{y,\epsilon}^{(\hat{x})}$ in the aforementioned indicator function. Consequently, we introduce a new indicator function,

$$W^{(\hat{x})}(y):=\left[\sum_{n=1}^{\infty}\frac{|\langle\phi_y^{(\hat{x})},\psi_n^{(\hat{x})}\rangle|^2_{L^2(0,K)}}{|\lambda_n^{(\hat{x})}|}\right]^{-1}\sim\left[\sum_{n=1}^{N}\frac{|\langle\phi_y^{(\hat{x})},\psi_n^{(\hat{x})}\rangle|^2_{L^2(0,K)}}{|\lambda_n^{(\hat{x})}|}\right]^{-1} \tag{4.2}$$

Copyright © by SIAM. Unauthorized reproduction of this article is prohibited.

Downloaded 06/21/24 to 60.29.153.12 . Redistribution subject to SIAM license or copyright; see https://epubs.siam.org/terms-privacy

Downloaded 06/21/24 to 60.29.153.12 . Redistribution subject to SIAM license or copyright; see https://epubs.siam.org/terms-privacy

for $y\in\mathbb{R}^3$, where the integer $N\in\mathbb{N}$ is a truncation number. Taking the limit $\epsilon\to 0$ in Theorem 4.1, it follows that

$$W^{(\hat{x})}(y)=\begin{cases}\geq 0 & \text{if} \quad y\in K_D^{(\hat{x})},\\ 0 & \text{if} \quad y\notin K_D^{(\hat{x})}.\end{cases} \tag{4.3}$$

Hence, the values of $W^{(\hat{x})}$ in the strip $K_D^{(\hat{x})}$ should be relatively bigger than those elsewhere. In the case of sparse observation directions $\{\hat{x}_j : j=1,2,\ldots,M\}$, we shall make use of the following indicator function:

$$W(y)=\left[\sum_{j=1}^{M}\frac{1}{W^{(\hat{x}_j)}(y)}\right]^{-1}=\left[\sum_{j=1}^{M}\sum_{n=1}^{N}\frac{|\langle\phi_y^{(\hat{x}_j)},\psi_n^{(\hat{x}_j)}\rangle|^2_{L^2(0,K)}}{|\lambda_n^{(\hat{x}_j)}|}\right]^{-1},\ y\in\mathbb{R}^3. \tag{4.4}$$

Define the Θ-convex hull of D associated with $\{\hat{x}_j : j=1,2,\ldots,M\}$ as $\Theta_D := \bigcap_{j=1,2,\cdots,M}K_D^{(\hat{x}_j)}$.

THEOREM 4.2. *We have $W(y)\geq 0$ if $y\in\Theta_D$ and $W(y)=0$ if $y\notin\Theta_D$.*

Proof. If $y\in\Theta_D$, then $y\in K_D^{(\hat{x}_j)}$ for all $j=1,2,\ldots,M$, yielding that $\hat{x}_j\cdot y\in\hat{x}_j\cdot D$. Hence, one deduces from Theorem 4.1 that $0\leq W^{(\hat{x}_j)}(y)<\infty$ for all $j=1,2,\ldots,M$, implying that $0\leq W(y)$. On the other hand, if $y\notin\Theta_D$, there must exist some unit vector $\hat{x}_l$ such that $y\notin K_D^{(\hat{x}_l)}$. Again, using Theorem 4.1, we get

$$[W^{(\hat{x}_l)}(y)]^{-1}=\sum_{n=1}^{\infty}\frac{|\langle\phi_y^{(\hat{x}_l)},\psi_n^{(\hat{x}_l)}\rangle|^2_{L^2(0,K)}}{|\lambda_n^{(\hat{x}_l)}|}=\infty,$$

which proves $W(y)=0$ for $y\notin\Theta_D$. ◻

The values of $W(y)$ are expected to be large for $y\in\Theta_D$ and small for those $y\notin\Theta_D$. Below we shall provide a physical interpretation of the proposed inversion algorithm and build up connections with the time-dependent inverse source problems. We first remark that the above factorization method with multi-frequency data carries over to near-field measurements in three dimensions. More precisely, the proposed factorization method can be slightly modified to get an image of the annular region

$$\tilde{K}_D^{(x)} := \{y\in\mathbb{R}^3 : \inf_{z\in D}|x-z|<|x-y|<\sup_{z\in D}|x-z|\}\subset\mathbb{R}^3 \tag{4.5}$$

for every fixed measurement position $|x|=R$. For this purpose we suppose $D\subset B_R$ for some $R>0$ and define the near-field operator $\mathcal{N}^{(x)} : L^2(0,K)\to L^2(0,K)$ by

$$(\mathcal{N}^{(x)}\phi)(\tau):=\int_0^K w(x,k_c+\tau-s)\,\phi(s)\,ds, \quad \tau\in(0,K), \tag{4.6}$$

where $x\in\partial B_R$ is a measurement position and $w\in H^2(B_R)$ is the solution to the Helmholtz equation (1.6). Following the proof of Theorem 2.1, we obtain a factorization of the near-field operator as $\mathcal{N}^{(x)}=\tilde{L}\tilde{T}\tilde{L}^*$, where $\tilde{L}=\tilde{L}_D^{(x)} : X_D\to L^2(0,K)$ is defined by

$$(\tilde{L}u)(\tau)=\int_{t_{\min}}^{t_{\max}}\int_D e^{i\tau(|x-y|+t)}u(y,t)\,dydt, \qquad \tau\in(0,K),$$

Copyright © by SIAM. Unauthorized reproduction of this article is prohibited.

Downloaded 06/21/24 to 60.29.153.12 . Redistribution subject to SIAM license or copyright; see https://epubs.siam.org/terms-privacy

for all $u \in X_D$, and the middle operator $\tilde{T}: X_D \to X_D$ is again a coercive multiplication operator defined by

$$(\tilde{T}u)(y,t) := \frac{e^{\mathrm{i}k_c(|x-y|+t)}}{\sqrt{32\pi^3}|x-y|}\, u(y,t)\, S(y,t), \qquad |x| = R.$$

Choose the test function

$$\tilde{\phi}_{y,\epsilon}^{(x)}(k) := \frac{1}{T\,|B_\epsilon(y)|} \int_{t_{\min}}^{t_{\max}} \int_{B_\epsilon(y)} \frac{e^{ik(|x-z|+t)}}{4\pi|x-z|}\, dz\, dt,$$

which tends uniformly to

$$\tilde{\phi}_y^{(x)}(k) := \frac{-i\, e^{\mathrm{i}k|x-y|}}{4\pi k|x-y|T} \left(e^{\mathrm{i}kt_{\max}} - e^{\mathrm{i}kt_{\min}}\right),$$

as $\epsilon \to 0$ for all $k \in [k_{\min}, k_{\max}]$. Introduce the indicator function

$$\widetilde{W}^{(x)}(y) := \left[\sum_{n=1}^{\infty} \frac{|\langle \tilde{\phi}_y^{(x)}, \tilde{\psi}_n^{(x)}\rangle|^2_{L^2(0,K)}}{|\tilde{\lambda}_n^{(x)}|}\right]^{-1}, \qquad y \in \mathbb{R}^3, \tag{4.7}$$

where $(\tilde{\lambda}_n^{(x)}, \tilde{\psi}_n^{(x)})$ is an eigensystem of the near-field operator $(\mathcal{N}^{(x)})_\#$. As the counterpart to (4.4), one can show in the near-field case that the following holds.

COROLLARY 4.1. *We have Range*$[(\mathcal{N}^{(x)})_\#^{1/2}] =$ *Range*$(\tilde{L}^{(x)})$ *for all* $x \in \partial B_R$. *The indicator* $\widetilde{W}^{(x)} \geq 0$ *in* $\tilde{K}_D^{(x)}$ *and vanishes identically in the exterior of* $\tilde{K}_D^{(x)}$.

Now we want to bridge this near-field indicator function with the time-domain signals of wave equations. In the near-field case, we suppose that the sparse data are given by $\{w(x_j,k) : x_j \in \partial B_R, k \in (k_{\min}, k_{\max})\}$, which can be considered as the inverse Fourier transform of the time-dependent data $\{U(x_j,t) : x_j \in \partial B_R, t \in (0,T)\}$ for some $T > 2R + t_{\max}$. The time-dependent signal $t \mapsto U(x,t)$ with a fixed $x \in \partial B_R$ has a compact support, because the source term is compactly supported in $\overline{D} \times [t_{\min}, t_{\max}]$. Physically, this can be explained by the Huygens principle in 3D. Since the wave speed has been normalized to be one, it is not difficult to observe that the arrival time point T_{arr} and the terminal time point T_{ter} of the signal recorded by the sensor at $|x| = R$ are

$$T_{arr} = t_{\min} + \inf_{z \in D} |x - z|, \qquad T_{ter} = t_{\max} + \sup_{z \in D} |x - z|,$$

respectively, where $[t_{\min}, t_{\max}]$ represents the duration period for source radiating. This explains why the minimum distance and maximum distance between a measurement position x and our target D (which are equivalent to the annulus $\tilde{K}_D^{(x)}$) can be recovered from the multi-frequency near-field data at $|x| = R$.

5. Numerical examples.

In this section, we present a couple of numerical examples in $\mathbb{R}^2$ and $\mathbb{R}^3$ to test the proposed factorization method with far-field and near-field measurements. All numerical examples are implemented by MATLAB.

5.1. Numerical implements with far-field measurements in $\mathbb{R}^2$.

We first describe the reconstruction procedure with multi-frequency far-field data over a single

Copyright © by SIAM. Unauthorized reproduction of this article is prohibited.

Downloaded 06/21/24 to 60.29.153.12 . Redistribution subject to SIAM license or copyright; see https://epubs.siam.org/terms-privacy

or multiple observation direction(s). Unless otherwise stated, we always assume $k_{\min} = 0$. With such a choice the far-field operator (2.1) can be simplified to be

$$(F^{(\hat{x})}\phi)(\tau) = \int_0^{k_{\max}} w^\infty(\hat{x}, \tau - s)\phi(s)ds, \quad L^2(0, k_{\max}) \to L^2(0, k_{\max}) \tag{5.1}$$

by taking $k_c = 0$ and $K = k_{\max}$; see Remark 2.1. In our numerical examples below, we consider $2N - 1$ wave-number samples $w^\infty(\hat{x}, k_n), n = 1, 2, \ldots, N,$, and $w^\infty(\hat{x}, -k_n), n = 1, 2, \ldots, N-1$, of the far field, where $k_n = (n-0.5)\Delta k$, $\Delta k := k_{\max}/N$. Using the $2N - 1$ samples of the far field in (5.1) and applying the midpoint rule, we obtain from (5.1) that

$$(F^{(\hat{x})}\phi)(\tau_n) \approx \sum_{m=1}^{N} w^\infty(\hat{x}, \tau_n - s_m)\phi(s_m)\Delta k,$$

where $\tau_n := n\Delta k$ and $s_m := (m - 0.5)\Delta k$, $n, m = 1, 2, \ldots, N$. Accordingly, a discrete approximation of $F^{(\hat{x})}$ is given by the Toeplitz matrix

$$F^{(\hat{x})} := \begin{pmatrix} w^\infty(\hat{x}, k_1) & \overline{w^\infty(\hat{x}, k_1)} & \cdots & \overline{w^\infty(\hat{x}, k_{N-2})} & \overline{w^\infty(\hat{x}, k_{N-1})} \\ w^\infty(\hat{x}, k_2) & w^\infty(\hat{x}, k_1) & \cdots & \overline{w^\infty(\hat{x}, k_{N-3})} & \overline{w^\infty(\hat{x}, k_{N-2})} \\ \vdots & \vdots & & \vdots & \vdots \\ w^\infty(\hat{x}, k_{N-1}) & w^\infty(\hat{x}, k_{N-2}) & \cdots & w^\infty(\hat{x}, k_1) & \overline{w^\infty(\hat{x}, k_1)} \\ w^\infty(\hat{x}, k_N) & w^\infty(\hat{x}, k_{N-1}) & \cdots & w^\infty(\hat{x}, k_2) & w^\infty(\hat{x}, k_1) \end{pmatrix} \Delta k,$$

where $\overline{w^\infty(\hat{x}, k_n)} = w^\infty(\hat{x}, -k_n)$, $n = 1, \ldots, N - 1$, and $F^{(\hat{x})}$ is an $N \times N$ complex matrix. For any point $y \in \mathbb{R}^2$ we define the test function vector $\phi_y^{(\hat{x})} \in \mathbb{C}^N$ from (3.4) by

$$\phi_y^{(\hat{x})} := \left(\frac{-\mathrm{i}}{T\tau_1}(e^{\mathrm{i}\tau_1 T} - 1)\, e^{-\mathrm{i}\tau_1 \hat{x}\cdot y}, \ \ldots, \ \frac{-\mathrm{i}}{T\tau_N}(e^{\mathrm{i}\tau_N T} - 1)\, e^{-\mathrm{i}\tau_N \hat{x}\cdot y} \right), \tag{5.2}$$

where $T = t_{max} - t_{min}$. Denoting by $\{(\tilde{\lambda}_n^{(\hat{x})}, \psi_n^{(\hat{x})}) : n = 1, 2, \ldots, N\}$ an eigensystem of the matrix $F^{(\hat{x})}$, one then deduces that an eigensystem of the matrix $(F^{(\hat{x})})_\# := |\mathrm{Re}\,(F^{(\hat{x})})| + |\mathrm{Im}\,(F^{(\hat{x})})|$ is $\{(\lambda_n^{(\hat{x})}, \psi_n^{(\hat{x})}) : n = 1, 2, \ldots, N\}$, where $\lambda_n^{(\hat{x})} := |\mathrm{Re}\,(\tilde{\lambda}_n^{(\hat{x})})| + |\mathrm{Im}\,(\tilde{\lambda}_n^{(\hat{x})})|$. A plot of $W^{(\hat{x})}(y)$ should yield a visualization of the strip $K_D^{(\hat{x})}$ (see (4.5)) containing the source support. In the following numerical examples, the frequency band is taken as $(0, 16\pi/6)$ with $k_{\max} = 16\pi/6$, $N = 16$, and $\Delta k = \pi/6$. The wave-number-dependent source term $f(x, k)$ is supposed to be given by (1.5). We always take $t_{\min} = 0$ and $t_{\max} = T = 0.1$ unless otherwise specified.

5.1.1. One observation direction. We first consider reconstruction of the strip $K_D^{(\hat{x})}$ from the multi-frequency far-field data $w^\infty(\hat{x}, \pm k_n)$. In Figure 2, we show a visualization of reconstructions of three sources supported on a kite-shaped domain at the observation direction $\hat{x} = (\cos\theta, \sin\theta)$ with the angle $\theta \in (0, 2\pi]$. The time-dependent source functions are chosen as $S(x, t)$ satisfying the positivity assumption (1.2). We choose $S(x, t) = 3(t + 1)$ and $\theta = \pi/4$ in Figure 2(a); $S(x, t) = 3x_1(t + 1)$ and $\theta = \pi/2$ in Figure 2(b); $S(x, t) = 3(x_1^2 + x_2^2 - 4)(t + 1)$ and $\theta = 3\pi/4$ in Figure 2(c). The boundary of D is also shown in the picture (pink solid line). (Color is available online.) As predicted by our theoretical results, the reconstructions nicely approximate the smallest strip $K_D^{(\hat{x})}$ perpendicular to the observation directions that contains the support.

Copyright © by SIAM. Unauthorized reproduction of this article is prohibited.

Downloaded 06/21/24 to 60.29.153.12 . Redistribution subject to SIAM license or copyright; see https://epubs.siam.org/terms-privacy

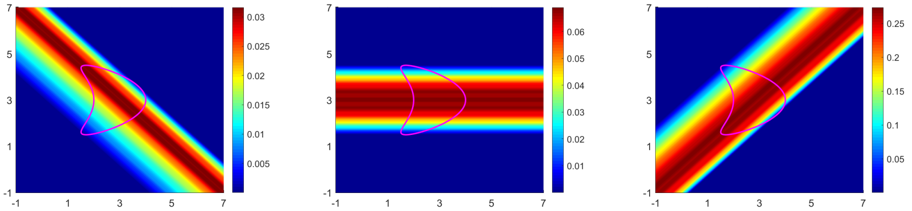

(a) $S=3(t+1), \theta=\pi/4$ (b) $S=3x_1(t+1), \theta=\pi/2$ (c) $S=3(x_1^2+x_2^2-4)(t+1), \theta=3\pi/4$

FIG. 2. *Reconstructions using a single observation direction and multi-frequency far-field data for a kite-shaped support. We choose* $t_{\min}=0$ *and* $t_{\max}=T=0.1$.

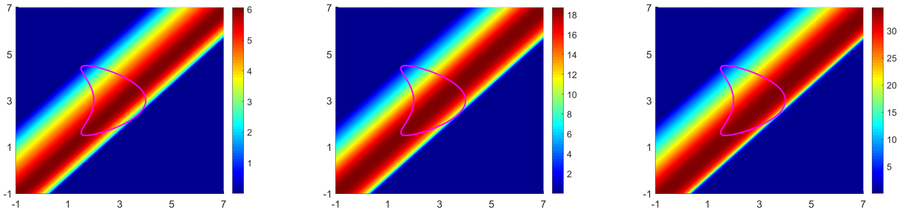

(a) $T=1$ (b) $T=2$ (c) $T=3$

FIG. 3. *Reconstructions of a kite-shaped support with* $S=3(x_1^2+x_2^2-4)(t+1)$ *and* $\theta=3\pi/4$ *with different inverse Fourier transform windows* $(0,T)$.

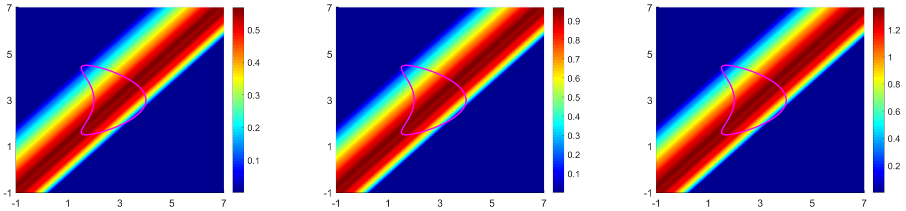

(a) $T_0=1, T=0.1$ (b) $T_0=2, T=0.1$ (c) $T_0=3, T=0.1$

FIG. 4. *Reconstructions of a kite-shaped support with* $S=3(x_1^2+x_2^2-4)(t+1)$, $\theta=3\pi/4$, *and with different inverse Fourier transform windows of the form* (T_0, T_0+T).

Next, we continue the numerical example for $S(x,t)=3(x_1^2+x_2^2-4)(t+1)$ and $\theta=3\pi/4$ in Figure 2(c) but with different inverse Fourier transform windows $(t_{\min}, t_{\max})$. We take $t_{\min}=0, t_{\max}=T$ with $T=1,2,3$ in Figure 3. The inverse Fourier transform window is taken to be $(t_{\min}, t_{\max})=(T_0, T_0+T)$ in Figure 4, with $T=0.1$ and $T_0=1,2,3$. In the last case, one needs to discretize the test vector (5.2). It is clearly shown that the source still lies in the smallest strip perpendicular to the observation direction. The numerical examples in Figures 3 and 4 show that our inversion algorithm is feasible for any $t_{\min}$ and $t_{\max}$.

5.1.2. Multiple observation directions. We present the reconstruction of a kite-shaped source using M observation directions with the observation angles $\theta_m=\frac{m-1}{M}\pi$, $m=1,\ldots,M$.

We show in Figure 5 a visualization of the reconstructed source with $S(x,t)=3(x_1^2+x_2^2)(t+1)$. Since the observation directions are perpendicular to each other

Copyright © by SIAM. Unauthorized reproduction of this article is prohibited.

Downloaded 06/21/24 to 60.29.153.12 . Redistribution subject to SIAM license or copyright; see https://epubs.siam.org/terms-privacy

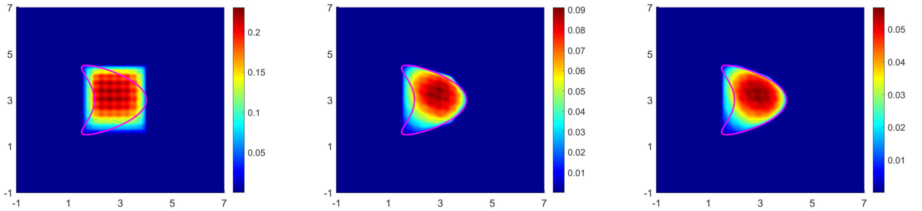

(a) $M=2$ (b) $M=5$ (c) $M=8$

FIG. 5. *Reconstructions of a kite-shaped source for* $S=3(x_1^2+x_2^2)(t+1)$ *with* M *observation directions. The inverse Fourier transform window* $(t_{\min},t_{\max})$ *is chosen as* $t_{\min}=0$ *and* $t_{\max}=0.1$.

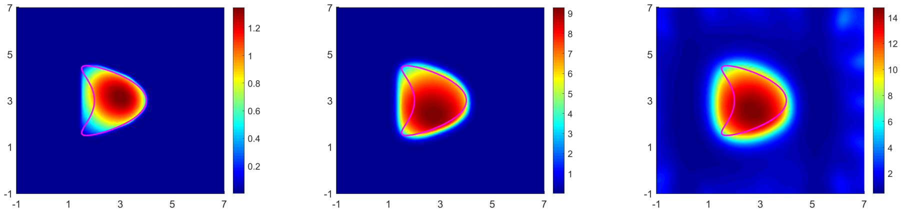

(a) $T=1$ (b) $T=5$ (c) $T=7$

FIG. 6. *Reconstructions from* $M=8$ *observation directions for a kite-shaped support. We choose* $S=3(x_1^2+x_2^2)(t+1)$ *and different inverse Fourier transform windows of the form* $(0,T)$.

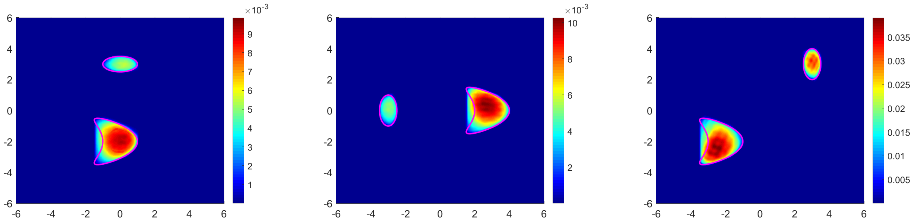

(a) $S=3(x_1+3)(t+1)$ (b) $S=3(x_2+3)(t+1)$ (c) $S=3(x_1^2+x_2^2)(t+1)$

FIG. 7. *Reconstructions of the shape of a source with two components from* 8 *observation directions. The inverse Fourier time window is* $(0,T)$ *with* $T=0.1$.

if $M=2$, the strips $K_D^{(\hat{x}_1)}$ and $K_D^{(\hat{x}_2)}$ are also perpendicular to each other as shown in Figure 5(a). It is clear that intersection of the strips contains the source support in Figure 5(a), (b), and (c), which approximates the convex hull of the support. Of course the number of observation directions affects reconstruction qualities: the more directions, the better the reconstructions.

We continue the numerical example in Figure 5(c) by choosing different inverse Fourier transform time windows $(0,T)$. The resulting reconstructions are shown in Figure 6 with three different choices $T=1,5,7$. The results are getting worse with increasing T, but they still contain useful information on the location and shape of the source support D. In all the other numerical examples, we take $T=0.1$ to get precise reconstructions.

Next we consider a source with two disconnected components: one component is kite-shaped and the other one is elliptic. We choose different source functions in Figure 7. It is shown that the two components are both precisely recovered using

Copyright © by SIAM. Unauthorized reproduction of this article is prohibited.

Downloaded 06/21/24 to 60.29.153.12 . Redistribution subject to SIAM license or copyright; see https://epubs.siam.org/terms-privacy

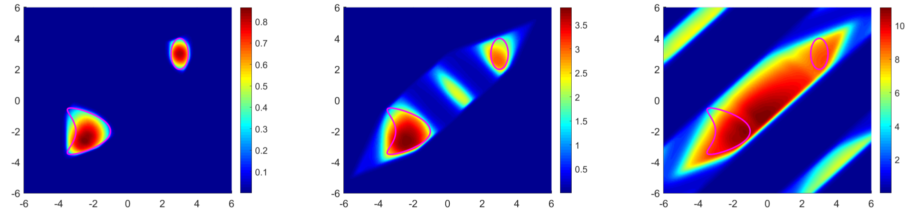

(a) $T = 1$ (b) $T = 3$ (c) $T = 5$

FIG. 8. *Reconstructions of two disjoint components from* 8 *observation directions with different time windows* $(0, T)$*. The source function is* $S = 3(x_1^2 + x_2^2)(t + 1)$*.*

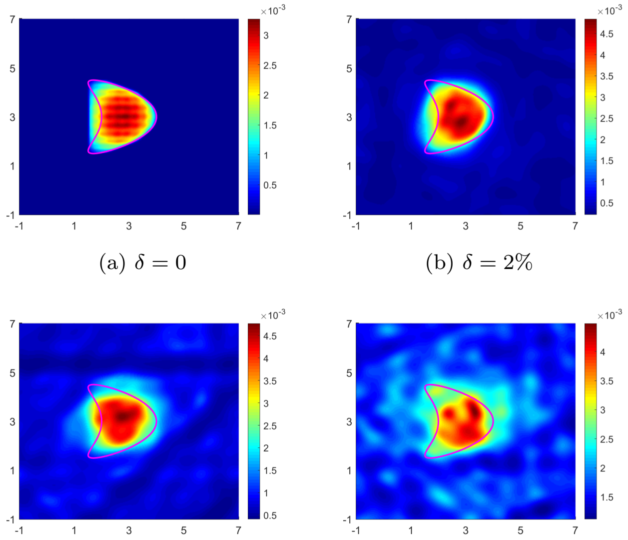

(a) $\delta = 0$ (b) $\delta = 2\%$

(c) $\delta = 5\%$ (d) $\delta = 10\%$

FIG. 9. *Reconstructions of a kite-shaped source from* 8 *observation directions with* $S = 3(t + 1)$ *at different noise levels* δ*.*

8 observation directions. It is worth mentioning that the inverse Fourier transform time widow $(0, T)$ should not be too big in this case. If T is increasing from 1 to 5, the images will be distorted; see Figure 8. This is due to the fact that the wave-fields radiated from the two components and received by the sensors cannot be split. Figure 8(b) can be improved if we increase the number of frequencies. However, if T is larger than the distance between the two components (see Figure 8(c)), the two components cannot be well separated. Instead, the convex hull of the union of these two components can be recovered.

To test the sensitivity of the algorithm with respect to measurement noise, we pollute the far-field data matrix by $F_\delta^{(\hat{x})} := F^{(\hat{x})} + \delta \, \|F^{(\hat{x})}\|_2 \, \mathcal{M}$, where δ is the noise level and $\mathcal{M} \in \mathbb{R}^{N \times N}$ is a uniformly distributed random matrix with the random variable ranging from -1 to 1. We present the reconstruction in the noise-free case in Figure 9(a). The resulting reconstructions are shown in Figure 9(b), (c), and (d) at three noise levels. The images are clearly getting distorted at higher noise levels, but the location of the source can still be well captured.

Copyright © by SIAM. Unauthorized reproduction of this article is prohibited.

Downloaded 06/21/24 to 60.29.153.12 . Redistribution subject to SIAM license or copyright; see https://epubs.siam.org/terms-privacy

5.2. Numerical implements with near-field measurements in $\mathbb{R}^3$. In the following numerical examples, the frequency band is also taken as $(0, 16\pi/6)$ with $k_{\max} = 16\pi/6, N = 16$, and $\Delta k = \pi/6$. Here we clarify that an iso-surface represents the points in three-dimensional space where the indicator function $\widetilde{W}(y)$ or $W(y)$ has a constant value and that an iso-surface level typically refers to a specific value of the indicator function $\widetilde{W}(y)$ or $W(y)$ in space. In the first example, we use the indicator function $\widetilde{W}^{(x)}(y)$ of (4.7) to reconstruct the annulus $\widetilde{K}_D^{(x)}$ in (4.5) for a cube. We take the temporal and spatial dependent source functions to be $F(x,t) = (x_1^2 + x_2^2 + x_3^2 + 1)(t+1)$ and the support of the source is assumed to be $\overline{D} \times [t_{\min}, t_{\max}]$. The cube D is defined by $D = \{(x_1, x_2, x_3) : |x_1| \leq 0.5, |x_2| \leq 0.5, |x_3| \leq 0.5\}$ (see Figure 10(a)). We take $t_{\min} = 0$, $t_{\max} = 0.1$ and set the measurement point at $(1.5, 0, 0)$. Then $\widetilde{W}^{(x)}(y)$ is plotted over the searching domain $[-1.5, 1.5]^3$ in Figure 10(b) and (c). We present a slice of the reconstruction at $y_2 = 0$ in Figure 10(b), from which we conclude that the cross of the plane $y_2 = 0$ with the smallest annulus containing the square (in pink) and centered at $x = (1.5, 0, 0)$ is nicely reconstructed. Figure 10(c) illustrates an iso-surface of the reconstruction at the iso-level 1×10^{-3}. The iso-surfaces perfectly enclose the cube-shaped support.

Next we continue the above test with multiple observation points. A visualization of the indicator function is shown in Figure 11 with six observation points $\{(1.5, 0, 0), (-1.5, 0, 0), (0, 1.5, 0), (0, -1.5, 0), (0, 0, 1.5), (0, 0, -1.5)\}$. Figure 11(a) presents an iso-surface of the reconstruction at the iso-level 5×10^{-3} and the projections of the images onto the oy_1y_2, oy_1y_3, and oy_2y_3 planes. It is clearly shown that projections are all squares $[-0.5, 0.5]^2$, justifying the accuracy of our 3D reconstructions. Figures 11(b) and (c) illustrate slices of the reconstructions at the planes $y_2, y_3 = 0$ and $y_1, y_2 = 0$ using the data at six observation points. These slices also confirm the accuracy of the 3D reconstructions.

In Figures 12 to 14, we show iso-surfaces and slices of the 3D reconstruction of the cubic source with a longer radiating period $(t_{\min}, t_{\max})$. Different *inverse* Fourier

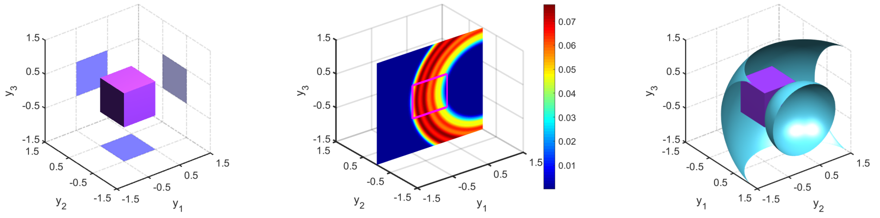

(a) Geometry of a cubic support (b) A slice at $y_2 = 0$ (c) Iso-surface level = 1×10^{-3}

FIG. 10. *Reconstructions of a cube from the data measured at one observation point* $(1.5, 0, 0)$.

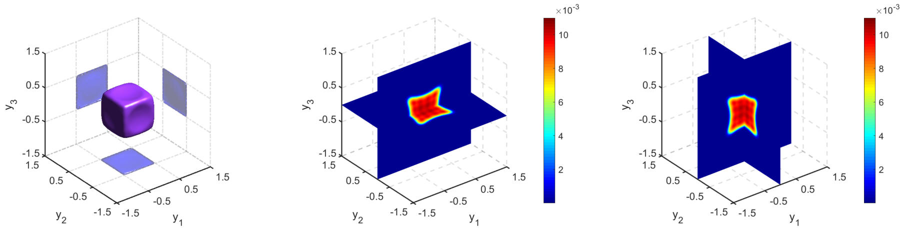

(a) Iso-surface level = 5×10^{-3} (b) Slices at $y_2, y_3 = 0$ (c) Slices at $y_1, y_2 = 0$

FIG. 11. *Reconstructions of a cube from six observation points.*

Copyright © by SIAM. Unauthorized reproduction of this article is prohibited.

Downloaded 06/21/24 to 60.29.153.12 . Redistribution subject to SIAM license or copyright; see https://epubs.siam.org/terms-privacy

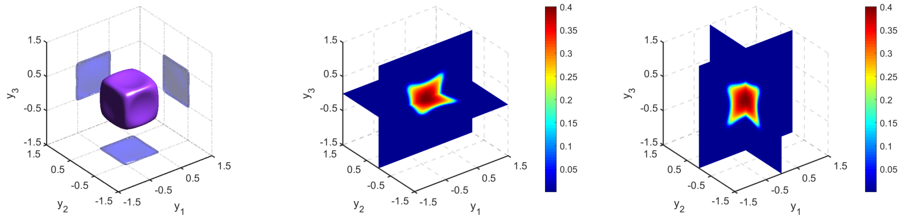

(a) Iso-surface level $=1.3\times10^{-1}$ (b) Slices at $y_2, y_3 = 0$ (c) Slices at $y_1, y_2 = 0$

FIG. 12. *Reconstructions of a cube from six observation points.*

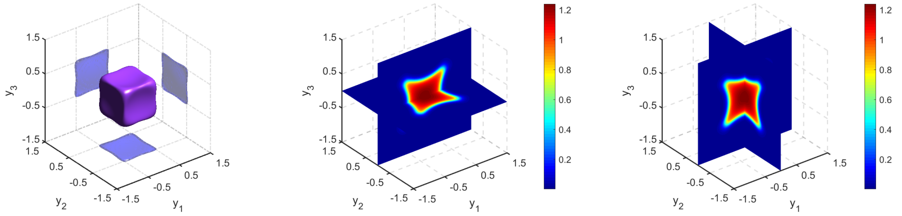

(a) Iso-surface level $= 9\times10^{-1}$ (b) Slices at $y_2, y_3 = 0$ (c) Slices at $y_1, y_2 = 0$

FIG. 13. *Reconstructions of a cube from six observation points.*

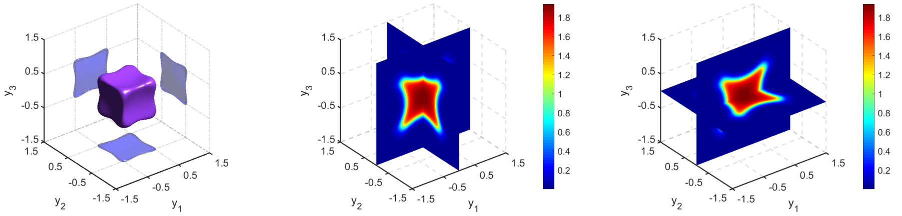

(a) Iso-surface level $= 1.6$ (b) Slices at $y_2, y_3 = 0$ (c) Slices at $y_1, y_2 = 0$

FIG. 14. *Reconstructions of a cube with six observation points.*

transform windows from the data measured at six observation points are used. We choose the radiating period (resp., inverse Fourier transform window) as $(0,1)$ in Figure 12, as $(0,3)$ in Figure 13, and as $(0,5)$ in Figure 14. It can be observed that, even for a long duration $T = t_{\max} - t_{\min}$, satisfactory inversions for capturing the shape and location of the source support D can be achieved by taking different iso-surface levels. We also present some slices of the reconstructions, which all confirm effectiveness of our algorithm.

5.3. Comparison between far-field and near-field measurements in $\mathbb{R}^3$. We continue to consider the example in subsection 5.2, where the exact geometry of the source support is cubic. Theoretically, the geometry can be exactly recovered using three properly chosen observation directions from the far-field measurements and approximately recovered using three properly chosen observation points in $\mathbb{R}^3$. In the numerical examples below, we choose $t_{\min} = 0$ and $t_{\max} = 0.1$. Using three observation directions $\hat{x} = \{(1,0,0),(0,1,0),(0,0,1)\}$ in Figure 15(a) from the far-field measurements, we can see that both the location and shape of the cubic source support

Copyright © by SIAM. Unauthorized reproduction of this article is prohibited.

Downloaded 06/21/24 to 60.29.153.12 . Redistribution subject to SIAM license or copyright; see https://epubs.siam.org/terms-privacy

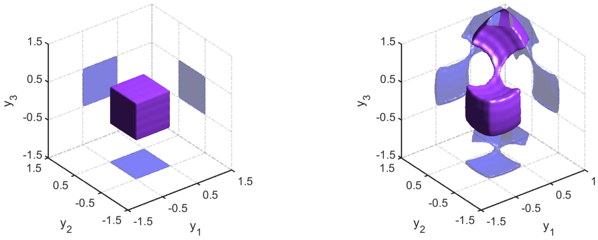

(a) Iso-surface level $= 2 \times 10^{-4}$ (b) Iso-surface level $= 1.4 \times 10^{-2}$

FIG. 15. *Reconstructions of a cube from three observation directions with the far-field measurements in* (a) *and from three observation points with the near field measurement in* (b).

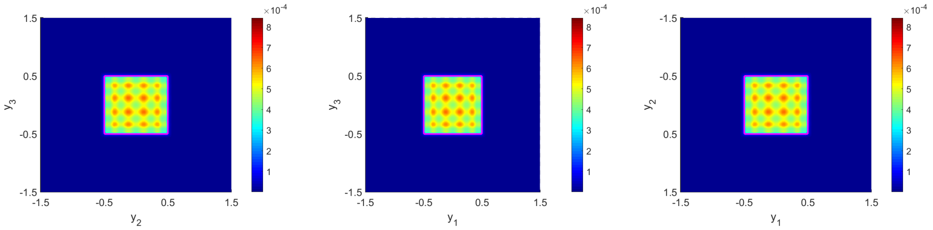

(a) A slices at $y_1 = 0$ (b) A slices at $y_2 = 0$ (c) A slices at $y_3 = 0$

FIG. 16. *Reconstructions of a cube with three observation directions for far-field case.*

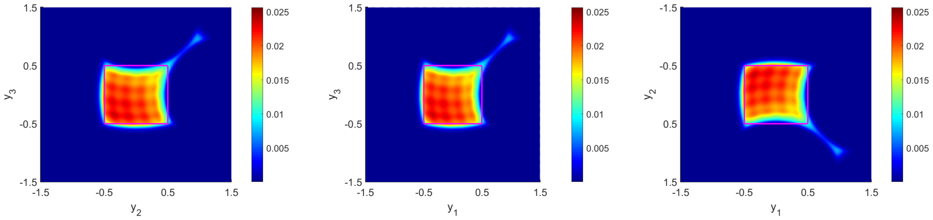

(a) A slices at $y_1 = 0$ (b) A slices at $y_2 = 0$ (c) A slices at $y_3 = 0$

FIG. 17. *Reconstructions of a cube with three observation points for near field case.*

are perfectly reconstructed just as our theoretical results predict. To clearly illustrate the reconstruction, we also plot the projections of the images onto the oy_2y_3, oy_1y_3, and oy_1y_2 planes. From the 2D visualizations one sees that the projections are all squares $[-0.5, 0.5]^2$. Figure 16 shows slices of the reconstruction at the planes $y_1 = 0$, $y_2 = 0$, and $y_3 = 0$. For comparison we also demonstrate the boundary of the source support slice with the pink solid line. These slices also confirm the accuracy of our algorithm. While using three observation points $x = \{(1.5, 0, 0), (0, 1.5, 0), (0, 0, 1.5)\}$ from the near-field measurement in Figure 15(b), we can see that only the location is captured, but the shape, which is not accurately reconstructed, is even severely disturbed. We also present slices of the reconstruction in Figure 17. The shape of the source support is well constructed, because the image is formed by the intersection of annulus (just as Figure 10(c)) centered at the three observation points respectively. However, in the far-field case with one observation point, the source support is located between two planes that are perpendicular to the observation direction.

Copyright © by SIAM. Unauthorized reproduction of this article is prohibited.

Acknowledgments. G. Hu acknowledges the hospitality of the Institute for Applied and Numerical Mathematics, Karlsruhe Institute of Technology, and the support of Alexander von Humboldt-Stiftung. Special thanks are given to R. Griesmaier for stimulating discussions.

REFERENCES

[1] R. Albanese and P. Monk, *The inverse source problem for Maxwell's equations*, Inverse Problems, 22 (2006), pp. 1023–1035.

[2] C. Alves, R. Kress, and P. Serranho, *Iterative and range test methods for an inverse source problem for acoustic waves*, Inverse Problems, 25 (2009), 055005.

[3] A. Alzaalig, G. Hu, X. Liu, and J. Sun, *Fast acoustic source imaging using multi-frequency sparse data*, Inverse Problems, 36 (2020), 025009.

[4] H. Ammari, G. Bao, and J. Fleming, *An inverse source problem for Maxwell's equations in magnetoencephalography*, SIAM J. Appl. Math., 62 (2002), pp. 1369–1382, https://doi.org/10.1137/S0036139900373927.

[5] A. Badia and T. Nara, *An inverse source problem for Helmholtz's equation from the Cauchy data with a single wave number*, Inverse Problems, 27 (2011), 105001.

[6] G. Bao, P. Li, J. Lin, and F. Triki, *Inverse scattering problems with multi-frequencies*, Inverse Problems, 31 (2015), 09300.

[7] G. Bao, J. Lin, and F. Triki, *A multi-frequency inverse source problem*, J. Differential Equations, 249 (2010), pp. 3443–3465.

[8] G. Bao, S. Lu, W. Rundell, and B. Xu, *A recursive algorithm for multi-frequency acoustic inverse source problems*, SIAM J. Numer. Anal., 53 (2015), pp. 1608–1628.

[9] G. Bao and F. Triki, *Error estimates for the recursive linearization for solving inverse medium problems*, J. Comput. Math., 28 (2010), pp. 725–744.

[10] E. Blasten, *Nonradiating sources and transmission eigenfunctions vanish at corners and edges*, SIAM J. Math. Anal., 6 (2018), pp. 6255–6270.

[11] N. Bleistein and J. Cohen, *Nonuniqueness in the inverse source problem in acoustics and electromagnetics*, J. Math. Phys., 18 (1977), pp. 194–201.

[12] J. Cheng, V. Isakov, and S. Lu, *Increasing stability in the inverse source problem with many frequencies*, J. Differential Equations, 260 (2016), pp. 4786–4804.

[13] A. J. Devaney and E. Wolf, *Radiating and non-radiating classical current distributions and the fields they generate*, Phys. Rev. D, 8 (1973), pp. 1044–1047.

[14] A. Devaney and G. Sherman, *Nonuniqueness in inverse source and scattering problems*, IEEE Trans. Antennas Propag., 30 (1982), pp. 1034–1037.

[15] M. Eller and N. Valdivia, *Acoustic source identification using multiple frequency information*, Inverse Problems, 25 (2009), 115005.

[16] A. C. Fannjiang, T. Strohmer, and P. Yan, *Compressed remote sensing of sparse objects*, SIAM J. Imaging Sci., 3 (2010), pp. 595–618, https://doi.org/10.1137/090757034.

[17] R. Griesmaire and C. Schmiedecke, *A factorization method for multifrequency inverse source problem with sparse far field measurements*, SIAM J. Imaging Sci., 10 (2017), pp. 2119–2139, https://doi.org/10.1137/17M111290X.

[18] R. Griesmaier, *Multi-frequency orthogonality sampling for inverse obstacle scattering problems*, Inverse Problems, 27 (2011), 085005.

[19] R. Griesmaier and M. Hanke, *Multifrequency impedance imaging with multiple signal classification*, SIAM J. Imaging Sci., 8 (2015), pp. 939–967, https://doi.org/10.1137/140992436.

[20] R. Griesmaier, M. Hanke, and T. Raasch, *Inverse source problems for the Helmholtz equation and the windowed Fourier transform*, SIAM J. Sci. Comput., 34 (2012), pp. A1544–A1562, https://doi.org/10.1137/110855880.

[21] R. Griesmaier, M. Hanke, and T. Raasch, *Inverse source problems for the Helmholtz equation and the windowed Fourier transform* II, SIAM J. Sci. Comput., 35 (2013), pp. A2188–A2206, https://doi.org/10.1137/130908658.

[22] R. Griesmaier, M. Hanke, and J. Sylvester, *Far field splitting for the Helmholtz equation*, SIAM J. Numer. Anal., 52 (2014), pp. 343–362, https://doi.org/10.1137/120891381.

[23] R. Griesmaier and C. Schmiedecke, *A multifrequency MUSIC algorithm for locating small inhomogeneities in inverse scattering*, Inverse Problems, 33 (2017), 035015.

[24] B. B. Guzina, F. Cakoni, and C. Bellis, *On the multi-frequency obstacle reconstruction via the linear sampling method*, Inverse Problems, 26 (2010), 125005.

Downloaded 06/21/24 to 60.29.153.12 . Redistribution subject to SIAM license or copyright; see https://epubs.siam.org/terms-privacy

Copyright © by SIAM. Unauthorized reproduction of this article is prohibited.

[25] H. Guo and G. Hu, *Inverse Wave-Number-Dependent Source Problems for the Helmholtz Equation*, arXiv:2305.07459v2, [math.NA], 2023.

[26] G. Hu, Y. Kian, P. Li, and Y. Zhao, *Inverse moving source problems in electrodynamics*, Inverse Problems, 35 (2019), 075001.

[27] G. Hu and Y. Kian, *Uniqueness and stability for the recovery of a time-dependent source in elastodynamics*, Inverse Probl. Imaging, 14 (2020), pp. 463–487.

[28] G. Hu, Y. Kian, and Y. Zhao, *Uniqueness to some inverse source problems for the wave equation in unbounded domains*, Acta Math. Appl. Sin. Engl. Ser., 36 (2020), pp. 134–150.

[29] M. Ikehata, *Reconstruction of a source domain from the Cauchy data*, Inverse Problems, 15 (1999), pp. 637–645.

[30] Z. Li, Y. Liu, J. Sun, and L. Xu, *Quality-Bayesian approach to inverse acoustic source problems with partial data*, SIAM J. Sci. Comput., 43 (2021), pp. A1062–A1080, https://doi.org/10.1137/20M132345X.

[31] D. R. Luke, *Multifrequency inverse obstacle scattering: The point source method and generalized filtered backprojection*, Math. Comput. Simul., 66 (2004), pp. 297–314.

[32] X. Ji, X. Liu, and B. Zhang, *Inverse acoustic scattering with phaseless far field data: Uniqueness, phase retrieval, and direct sampling methods*, SIAM J. Imaging Sci., 12 (2019), pp. 1163–1189, https://doi.org/10.1137/18M1236022.

[33] X. Ji, X. Liu, and B. Zhang, *Target reconstruction with a reference point scatterer using phaseless far field patterns*, SIAM J. Imaging Sci., 12 (2019), pp. 372–391, https://doi.org/10.1137/18M1205789.

[34] X. Ji, X. Liu, and B. Zhang, *Phaseless inverse source scattering problem: Phase retrieval, uniqueness and direct sampling methods*, J. Comput. Phys. X, 1 (2019), 100003.

[35] A. Kirsch, *Characterization of the shape of a scattering obstacle using the spectral data of the far field operator*, Inverse Problems, 14 (1998), pp. 1489–1512.

[36] A. Kirsch, *The MUSIC algorithm and the factorization method in inverse scattering theory for inhomogeneous media*, Inverse Problems, 18 (2002), pp. 1025–1040.

[37] A. Kirsch and N. Grinberg, *The Factorization Method for Inverse Problems*, Oxford University Press, Oxford, UK, 2008.

[38] S. Kusiak and J. Sylvester, *The scattering support*, Comm. Pure Appl. Math., 56 (2003), pp. 1525–1548.

[39] P. Li and G. Yuan, *Increasing stability for the inverse source scattering problem with multifrequencies*, Inverse Probl. Imaging, 11 (2017), pp. 745–759.

[40] G. Ma and G. Hu, *Factorization method with one plane wave: From model-driven and data-driven perspectives*, Inverse Problems, 38 (2022), 015003.

[41] R. Potthast, *A study on orthogonality sampling*, Inverse Problems, 26 (2010), 074015.

[42] M. Sini and N. Thanh, *Inverse acoustic obstacle scattering problems using multifrequency measurements*, Inverse Probl. Imaging, 6 (2012), pp. 749–773.

[43] J. Sylvester, *Notions of support for far fields*, Inverse Problems, 22 (2006), pp. 1273–1288.

[44] J. Sylvester and J. Kelly, *A scattering support for broadband sparse far field measurements*, Inverse Problems, 21 (2005), pp. 759–771.

[45] D. Zhang and Y. Guo, *Fourier method for solving the multi-frequency inverse source problem for the Helmholtz equation*, Inverse Problems, 31 (2015), 035007.

Downloaded 06/21/24 to 60.29.153.12 . Redistribution subject to SIAM license or copyright; see https://epubs.siam.org/terms-privacy

Copyright © by SIAM. Unauthorized reproduction of this article is prohibited.